Yan *et al. Chem. Synth.* **2025**, *5*, 26
DOI: 10.20517/cs.2024.35

Chemical Synthesis

Research Article

Open Access

Check for updates

Synergistic promotion of ultra-small Pt nanoparticles and oxygen vacancy in MOF catalyst for ethyl levulinate to valerolactone at room temperature

Wei Yan[1], Ying Wang[1,*], Xu Zhao[2], Siyi Pu[1], Chunyan Yang[1], Zirui Dao[1], Changfu Zhuang[1], Chungang Min[3,*], Xiao-Jun Zhao[4,*], Xiaoqin Zou[2,*]

[1]Key Laboratory of Forest Resources Conservation and Utilization in the Southwest Mountains of China Forestry and Grassland Administration, Southwest Forestry University, Kunming 650051, Yunnan, China.
[2]Faculty of Chemistry, Northeast Normal University, Changchun 130024, Jilin, China.
[3]Research Center for Analysis and Measurement, Kunming University of Science and Technology, Kunming 650093, Yunnan, China.
[4]Key Laboratory of Advanced Materials of Tropical Island Resources, Ministry of Education, School of Chemistry and Chemical Engineering, Hainan University, Haikou 570228, Hainan, China.

[*]**Correspondence to:** Prof. Ying Wang, Key Laboratory of Forest Resources Conservation and Utilization in the Southwest Mountains of China Forestry and Grassland Administration, Southwest Forestry University, No. 300, Bailong Temple, Qingyun Street, Kunming 650051, Yunnan, China. E-mail: yingwang@swfu.edu.cn; Prof. Chungang Min, Research Center for Analysis and Measurement, Kunming University of Science and Technology, No. 68 Xuefu Road, Kunming 650093, Yunnan, China. E-mail: minchungang@163.com; Dr. Xiao-Jun Zhao, Key Laboratory of Advanced Materials of Tropical Island Resources, Ministry of Education, School of Chemistry and Chemical Engineering, Hainan University, No. 58 Renmin Avenue, Haikou 570228, Hainan, China. E-mail: xiaojunzhao2013@163.com; Prof. Xiaoqin Zou, Faculty of Chemistry, Northeast Normal University, No. 5268 Renmin Street, Changchun 130024, Jilin, China. E-mail: zouxq100@nenu.edu.cn

How to cite this article: Yan, W.; Wang, Y.; Zhao, X.; Pu, S.; Yang, C.; Dao, Z.; Zhuang, C.; Min, C.; Zhao, X. J.; Zou, X. Synergistic promotion of ultra-small Pt nanoparticles and oxygen vacancy in MOF catalyst for ethyl levulinate to valerolactone at room temperature. *Chem. Synth.* **2025**, *5*, 26. https://dx.doi.org/10.20517/cs.2024.35

Received: 16 Mar 2024 **First Decision:** 6 Jun 2024 **Revised:** 21 Jun 2024 **Accepted:** 8 Jul 2024 **Published:** 17 Feb 2025

Academic Editor: Ying Wan **Copy Editor:** Pei-Yun Wang **Production Editor:** Pei-Yun Wang

Abstract

Currently, designing highly efficient catalysts for biomass hydrogenation at low temperatures remains a significant challenge. This paper proposes a straightforward solvent-treatment strategy to create rich oxygen vacancies (O_V), facilitating the loading of ultra-small (1.6 nm) Pt nanoparticles (NPs) onto a metal-organic framework (MOF) (LaQS) with rich O_V (LaO_V-r). Consequently, a bifunctional Pt_2/LaO_V-r catalyst, featuring Lewis acid and metal hydrogenation sites, was synthesized. Under mild conditions (80 °C), the Pt_2/LaO_V-r catalyst exhibited a catalytic

yield of >99% in converting biobased ethyl acetylpropionate [ethyl levulinate (EL)] to valerolactone [γ-valerolactone (GVL)]. This yield was 3.2 and 13.3 times higher than those measured by Pt_2/LaQS and commercial Pt/C catalysts, respectively. Specifically, Pt_2/LaO_V-r catalyzed the full conversion of EL to GVL even at room temperature. The results revealed that the synergistic effect between ultra-small Pt NPs and O_V in the MOF catalyst is important for the efficient conversion of EL into GVL. Especially, the abundant O_V defects in LaO_V-r not only enhanced the electron cloud density of Pt NPs at active sites of hydrogenation, but also elevated the content of moderately-strong acidic sites. This enhances the ability to activate H_2 and EL, and promotes the intra-molecular dehydration of intermediates to GVL. The synergistic catalytic mechanism of O_V and ultra-small Pt NPs in MOFs is proposed. This study presents an effective strategy for defect engineering aimed at enhancing catalytic biomass conversion using MOFs-loaded metal NPs.

Keywords: Metal organic frameworks, ultra-small Pt NPs, oxygen vacancy, catalysis, ethyl acetylpropionate, valerolactone

INTRODUCTION

Hydrogenation to produce fuels and chemicals is an important way to realize the value of biomass[1,2]. Levulinic acid (LA) is considered one of the twelve most important biomass platform molecules[3,4]. LA can be transformed into many high-value derivatives[2,3,5]. Among these, γ-valerolactone (GVL) stands out as a pivotal bioplatform molecule, offering versatility for diverse applications[6-10]. The catalytic hydrogenation of LA and ethyl acetylpropionate [ethyl levulinate (EL)] is considered the primary route for GVL production[9,11-15]. The relatively low boiling point of EL compared to LA enhances catalyst stability and reduces the risk of reaction vessel corrosion. However, the hydrogenation process from EL to GVL still faces problems such as complicated catalyst preparation and poor cycle stability. In particular, the catalytic efficiency is low at lower temperatures. Therefore, a thorough study is needed to find an efficient catalytic system for preparing GVL.

Precious metal catalysts (such as Pt, Pd, Ru, *etc.*), especially Pt-based catalysts have excellent capabilities of activating hydrogen and carbonyl[16-21]. However, currently Pt-based catalysts typically require higher hydrogen pressure (2.5-6 MPa)[22-24] and/or elevated reaction temperature (≥150 °C)[25,26]. Therefore, it is necessary to develop Pt-based catalytic systems for GVL preparation under mild conditions. The development of bifunctional catalysts is crucial in light of the fact that EL undergoes reduction followed by dehydration to generate GVL. Among them, the metal site facilitates C=O reduction, and the acidic site influences intermediate conversion and reactant adsorption[17,27-29]. Therefore, simultaneous tuning of both hydrogenation and Lewis acidic sites in Pt-based catalysts is imperative.

Generally, the sizes of metal nanoparticles (NPs) and the interaction of metal-support play a significant role in determining the catalytic performance[30,31]. However, the small metal particle size does not significantly enhance catalyst performance in hydrogenation reactions, particularly at low temperatures[32]. Therefore, controlling the interaction between metal and support becomes a crucial factor in regulating hydrogenation activity. In recent years, metal-organic frameworks (MOFs) have garnered considerable attention as catalyst supports due to their high specific surface areas, diverse structures and customizable functionalities[33]. Although the functional synergy between metal NPs and MOFs has been extensively investigated, resulting in remarkable catalytic performance. However, it is regrettable that the majority of activity originates from the metal NPs alone, which undermines the potential contribution of MOFs[34]. MOFs are considered to help reactant molecules to activate/regulate surface properties of metal NPs[35]. Therefore, the integration of MOFs with metal NPs holds great promise for harnessing synergistic catalytic effects.

Defect engineering is an effective strategy for tuning the performance of MOFs-based catalysts[36,37]. Previous studies have demonstrated that the introduction of defects in MOFs not only enhanced porosity and generated many open metal sites, but also facilitated the anchoring of metal NPs, regulating electronic structure and increasing active sites of the catalyst[38,39]. MOFs-based catalysts with abundant defects exhibit enhanced adsorption and activation capabilities towards reactants and intermediates[40]. Additionally, facile synthetic methods and improved durability are pivotal factors for practical applications of NPs/MOFs catalysts[34]. However, the current materials primarily consist of a limited combination of metal NPs and well-known MOFs, such as UiO-66 and ZIF-8[35]. So, it is still a big challenge to develop hybrid materials of MOFs with high thermal stability and metal NPs. Moreover, the methods reported for MOFs defect regulation are relatively few and complex. Therefore, there is an urgent need to develop a simple and effective method to solve the above problems.

This study presents a concise $NaBH_4$ room-temperature treatment strategy for preparing bifunctional catalyst (Pt_2/LaO_V-r) with ultra-small metal NPs and rich oxygen vacancies (O_V). When Pt_2/LaO_V-r was used to convert EL to GVL, excellent catalytic results were obtained. In particular, complete conversion was also achieved at room temperature. The synergistic promotion of metal NPs and O_V in MOFs support was explored through characterization and theoretical calculations.

EXPERIMENTAL

Materials

Methanol (99.7%), ethanol (99.7%), 2-propanol (99.7%), ethylenediamine (99.7%), dichloromethane (99.7%), $NaBH_4$ (99.7%) and N,N-dimethylformamide (DMF) (99.7%) were purchased from Sinopharm Chemical Reagent Co. EL (99.0%) and $LaCl_3{\cdot}xH_2O$ (99.0%) were purchased from Adamas Reagent Co. $H_2PtCl_6{\cdot}6H_2O$ and 8-hydroxyquinoline-5-sulfonic acid (H_2QS) were procured from TCI (Shanghai).

Catalyst characterization

Powder X-ray diffraction (XRD) patterns were obtained using a Rigaku Ultima XRD spectrometer with Cu Kα radiation (λ = 1.5418 Å) at 40 kV and 40 mA. The specific surface areas and pore properties of catalysts were determined using the Brunauer-Emmett-Teller (BET) method at 77 K with a Micromeritics ASAP 2460 physical adsorption instrument for N_2 adsorption-desorption measurements. Transmission electron microscopy (TEM) and high-resolution TEM (HR-TEM) were conducted using a JEM-2100 instrument at 200 kV. X-ray photoelectron spectroscopy (XPS) analysis was performed with a monochromatic Al Kα X-ray source at 50 W, 15 kV on a PHI5000 Versaprobe II scanning XPS microprobe system. XPS spectra were fitted on the software MultiPeak to analyze the elemental compositions and chemical species of the samples, with binding energy based on a C 1s peak at 284.8 eV. Temperature-programmed desorption (TPD)/temperature-programmed reduction (TPR) of H_2, CO_2 and NH_3 were performed using a Quzhou Ward VDSorb-91i instrument. Electron paramagnetic resonance (EPR) tests were conducted at room temperature with a Bruker EMXPLUS spectrometer. The metal contents of the samples were determined by inductively coupled plasma emission spectrometry (ICP-OES) with a VISTA-MPX instrument. Raman spectroscopy (Raman) was employed to examine the molecular states of the samples with a WITec alpha300R instrument from Germany. Fourier Transform infrared spectroscopy (FT-IR) was performed using a Bruker Optik Gmbh tensor 27 spectrometer in Germany. *In situ* CO adsorption infrared spectroscopy was conducted using a Bruker VERTEX 80 V FT-IR spectrometer programmed at 5 °C/min from room temperature to 80 °C, with a N_2 airflow purge for 30 min as pretreatment.

Synthesis of catalysts

The catalysts were prepared by loading ultra-small Pt NPs using the impregnation method. The LaQS support was synthesized by reacting $LaCl_3{\cdot}xH_2O$ and H_2QS under solvothermal conditions. The 1.22 g

$LaCl_3 \cdot xH_2O$ and 0.8 g H_2QS were dissolved in 50 mL of DMF, and about 1 mL of ethylenediamine was added while stirring at room temperature. After 30 min, the mixture was transferred to a 100 mL Polytetrafluoroethylene (PTFE)-lined stainless steel autoclave and heated under autogenous pressure at 100 °C for 48 h. The yellow solid was filtered out, washed with ethanol and methanol, soaked in dichloromethane for one day, and then dried at 100 °C in a vacuum oven. After drying, the prepared LaQS (0.4 g) was added into the water (40 mL) with another stirring for 20 min. To prepare the Pt precursor, 0.024 g of chloroplatinic acid ($H_2PtCl_6 \cdot 6H_2O$) was placed in the water (20 mL) and sonicated for 5 min. For the preparation of Pt_2/LaO_V catalyst, the $NaBH_4$ solution (20 mL, 0.5 mol/L) was added slowly to the LaQS precursor with another stirring for 3 h. The Pt precursor was dropped into the LaQS aqueous solution with stirring for 3 h. Then, the $NaBH_4$ solution (20 mL, 0.5 mol/L) was added slowly with stirring for 3 h. Finally, filtered solids were dried in a tube furnace under argon at 80 °C to give Pt_2/LaO_V-r.

Method for catalytic performance evaluation

The hydrogenation of EL is carried out in a 25 mL reactor with high pressure. Normally, 25 mg of Pt_2/LaO_V-r was added to the PTFE liner followed by 1 mmol of ethyl acetylpropionate. The gas in the reactor was replaced five times with H_2, which was used to remove air from the reactor, and then the pressure was raised to 2 MPa. After the above steps were completed, the reaction time and temperature were set and the reaction was performed at a stirring rate of 800 rpm for the entire course of the reaction.

At the end of the reaction, the mixture was cooled to a lower temperature and the catalyst particles were filtered out of the solution using a filter membrane. The reacted catalyst was placed on a filtration unit and washed with ethanol, and dried at the end of filtration for subsequent cycling experiments. Reactants in the liquid phase were identified by gas chromatography-mass spectrometry (GC-MS, GCMS-QP2010 SE, Shimadzu) while the reaction samples were analyzed by GC (GC-7890A, Agilent). The reactant conversion and product selectivity are calculated as follows:

$$\text{Conversion (\%)} = \frac{\text{Mole of reactant transformed}}{\text{Number of moles of reactants loaded}} \times 100\% \quad (1)$$

$$\text{Selectivity (\%)} = \frac{\text{Number of GVL moles generated}}{\text{Number of moles of all products manufactured}} \times 100\% \quad (2)$$

RESULTS AND DISCUSSION

Material characterization

Synthesis of LaO_V-r anchored Pt NPs

Figure 1A is a schematic diagram of the preparation process of Pt_2/LaO_V-r. Firstly, a highly stable La-MOF (LaQS) was synthesized by hydrothermal method[41]. Then, LaQS support was treated by simple $NaBH_4$ solution at room temperature to form O_V-rich LaQS (LaO_V-r). Then, LaO_V-r was impregnated by Pt ions with subsequent $NaBH_4$ reduction at room temperature to give Pt_2/LaO_V-r with ultrafine Pt NPs. Meanwhile, a control sample (Pt_2/LaQS) was prepared by the same method using pristine LaQS.

XRD characterization was performed to confirm the structural integrity of the catalyst support. Figure 1B shows that the characteristic peaks in XRD patterns of Pt_2/LaO_V-r, Pt_2/LaQS and LaO_V-r match well with those of the parent LaQS. Additionally, they show good agreement with the simulated XRD characteristic peaks of LaQS. The structure of LaQS remains stable whether loaded after the vacancy treatment or directly loaded. Moreover, the content of the loading metal has little effect on the structure of LaQS [Supplementary Figure 1]. Diffraction peaks attributed to Pt NPs are challenging to be observed in Pt_2/LaO_V-r and Pt_2/LaQS by XRD. This difficulty may arise from the good dispersion of small-sized Pt NPs or low metal Pt content.

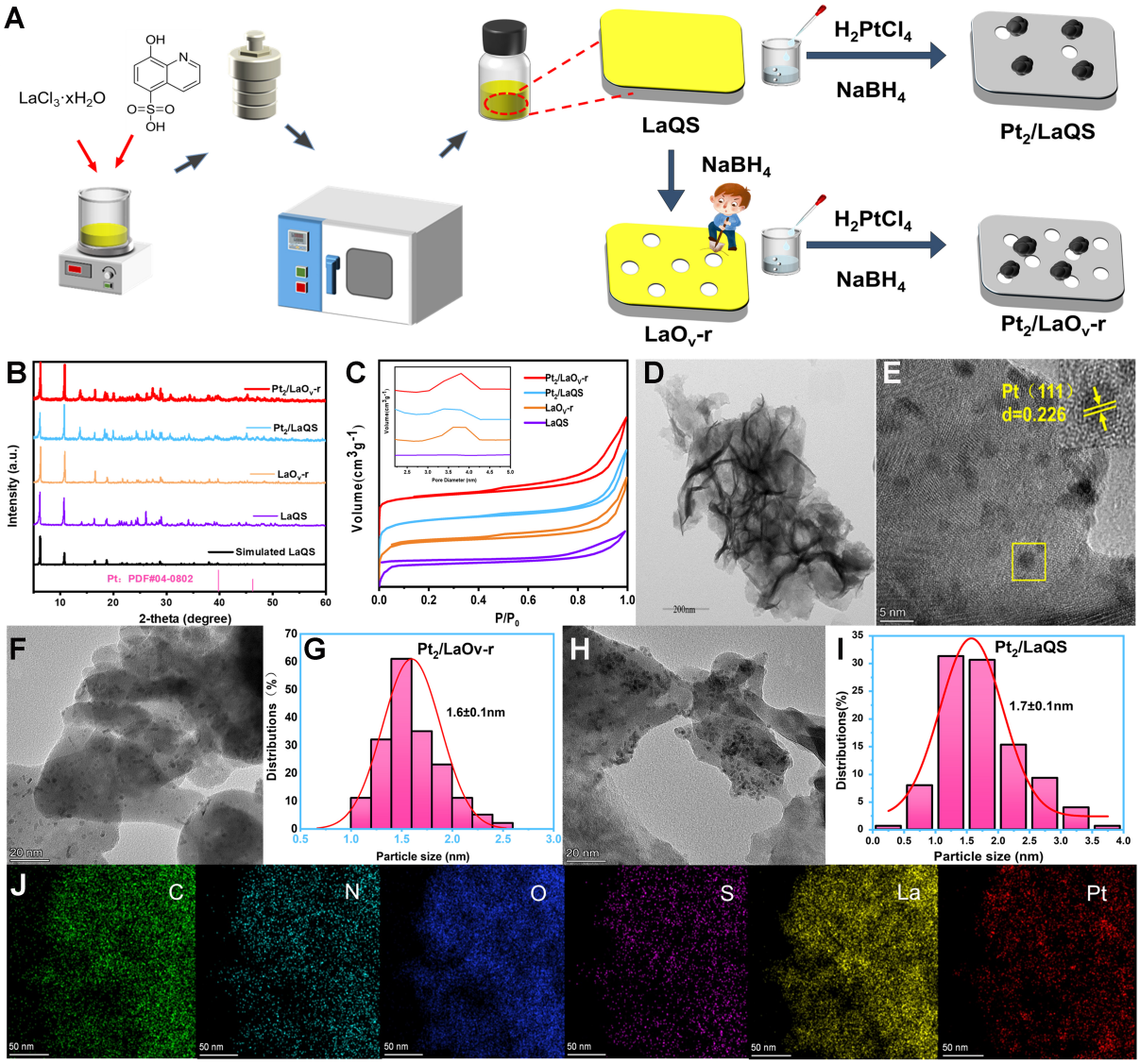

Figure 1. (A) Route for the preparation of LaQS, Pt_2/LaO_V-r and Pt_2/LaQS; (B and C) XRD patterns and N_2 adsorption isotherms of LaQS, LaO_V-r, Pt_2/LaQS and Pt_2/LaO_V-r; (D) TEM images of LaQS; (E) Lattice fringes and crystalline surfaces of Pt in Pt_2/LaO_V-r; (F and G) TEM particle images and grain sizes of Pt_2/LaO_V-r; (H and I) TEM particle images and grain sizes of Pt_2/LaQS; (J) HR-TEM image and EDS elemental mapping of Pt_2/LaO_V-r. XRD: X-ray diffraction; TEM: transmission electron microscopy; HR-TEM: high-resolution TEM; EDS: energy dispersive X-ray spectroscopy.

N_2 sorption tests were employed to compare the porous structures of the catalysts. Figure 1C illustrates that all samples exhibit typical hysteresis loops, indicative of a type IV adsorption-desorption isotherm. This confirms the mesoporous structure. Meanwhile, as shown in Table 1, compared with LaQS (843.37 m^2/g), the Langmuir specific surface area of LaO_V-r with more vacancies is decreased to 512.25 m^2/g. An increase of O_V probably destroys some pores. The surface area provides abundant binding sites for Pt NPs. Compared with Pt_2/LaQS (603.56 m^2/g), the specific surface area of Pt_2/LaO_V-r after $NaBH_4$ treatment is decreased to 327.03 m^2/g, mainly due to the occupation of the pore space by Pt NPs.

Firstly, LaQS support with high specific surface area has a sheet structure [Figure 1D], which offers more sites for the adsorption of metallic Pt NPs. Secondly, the abundant O_V on LaO_V-r support have a positive

Table 1. The specific surface area, pore volume, pore size, Pt particle size, Pt species proportion, O_V content and Pt content of different catalysts

Sample	S_{BET} ($m^2 \cdot g^{-1}$)[a]	Pore volume ($cm^3 \cdot g^{-1}$)[a]	Pore size (nm)[a]	Pt particle size (nm)	Pt^0 (%)[b]	Pt^{4+} (%)[b]	O_V (%)[b]	Pt (wt%)[c]
LaQS	843.37	0.34	6.80	-	-	-	24.61	-
Pt_2/LaQS	603.56	0.35	11.99	1.7 ± 0.1	75.18	24.82	37.15	1.4
LaO_V-r	512.25	0.27	8.70	-	-	-	31.53	-
Pt_2/LaO_V-r	327.03	0.27	11.44	1.6 ± 0.1	65.97	34.03	44.35	1.6
Pt/C	2,745.39	1.06	3.43	-	76.18	23.82	26.70	5.0

[a]By N_2 adsorption. [b]By XPS analysis. [c]By ICP analysis. BET: Brunauer-Emmett-Teller; XPS: X-ray photoelectron spectroscopy; ICP: inductively coupled plasma.

effect on metal Pt dispersion. Importantly, the large π bond of the quinoline ring on the surface of the LaQS support interacts with Pt NPs. This is further proved by infrared spectroscopy (IR) and XPS analysis. The lattice stripe of 0.226 nm is clearly seen in Figure 1E, which corresponds to the crystal plane of single crystal Pt (111) (PDF#04-0802)[42]. It can be seen from the TEM images of Figure 1F-I that the particle size of the metal on Pt_2/LaO_V-r with rich O_V is only about 1.6 nm, which is almost the same as that of Pt_2/LaQS (1.7 nm). The uniform distribution of platinum metal on the support may be attributed to the following reasons. According to the energy dispersive X-ray spectroscopy (EDS) element mapping of Pt_2/LaO_V-r [Figure 1J], the O, N, S, C, La and Pt components are structurally uniformly distributed, and the highly overlapping elements also attest to the homogeneous dispersion of Pt on the vacancy-rich LaO_V-r support.

Interaction between LaO_V-r support and ultra-small Pt NPs

Figure 2A displays O_V peaks at g = 2.003 for LaQS, Pt_2/LaO_V-r, Pt_2/LaQS and LaO_V-r in EPR spectra. Among these, the peak area of Pt_2/LaO_V-r is larger than that of Pt_2/LaQS, indicating a significantly higher number of O_V in Pt_2/LaO_V-r. Similarly, the number of O_V in LaO_V-r is also higher than that in LaQS. This is further supported by the XPS analysis of oxygen [Figure 2B]. Compared with 532.42 eV on Pt_2/LaQS, the binding energy of O_V on Pt_2/LaO_V-r is increased to 532.73 eV. The binding energies of O_V on Pt_2/LaO_V-r and Pt_2/LaQS increase by 0.36 and 0.05 eV, compared with 532.37 and 532.31 eV for LaO_V-r and LaQS, respectively. This trend is consistent with the binding energy of N 1s in Figure 2C and of S 2P in Figure 2D. This suggests that with O_V increase, more electrons are transferred from O/N elements on the support to the metal Pt. Figure 2E demonstrates that the binding energy of La remains constant, suggesting that La–O bond breaking is not responsible for O_V generation. Combined with LaQS structure[41], this finding supports that O_V are primarily generated by S–O bond breaking.

FT-IR [Figure 2F] was employed to analyze the interactions of the O_V-rich Pt_2/LaO_V-r and Pt_2/LaQS with the support (LaO_V-r and LaQS). Compared with LaQS, the 1,660 cm^{-1} belongs to the C=C stretching vibration of the quinoline ring in LaO_V-r. The C=C bond on quinoline rings is destroyed when O_V is generated. Further, the C=C bands of Pt_2/LaO_V-r and Pt_2/LaQS are smaller. Another reason may be the interaction of Pt with the C=C conjugated system of the quinolyl ring. Moreover, the bands of 1,564 and 1,461 cm^{-1} belonging to the C=N stretching vibration of the quinoline ring in Pt_2/LaO_V-r are decreasing. Meanwhile, compared with LaQS and LaO_V-r, the band attributed to S–O vibration (690 and 600 cm^{-1}) on Pt_2/LaO_V-r and Pt_2/LaQS are greatly reduced. The possible reason is that the electron-rich S=O and C=N groups in LaQS and LaO_V-r interact with Pt NPs through π–π bonds. This interaction of metal with conjugated quinoline ring leads to the high dispersion of Pt NPs. Compared with Pt_2/LaQS, the above characteristic bands of Pt_2/LaO_V-r decrease more obviously with O_V, indicating that O_V also interacts with Pt NPs. This finding is consistent with the XPS and TEM analyses.

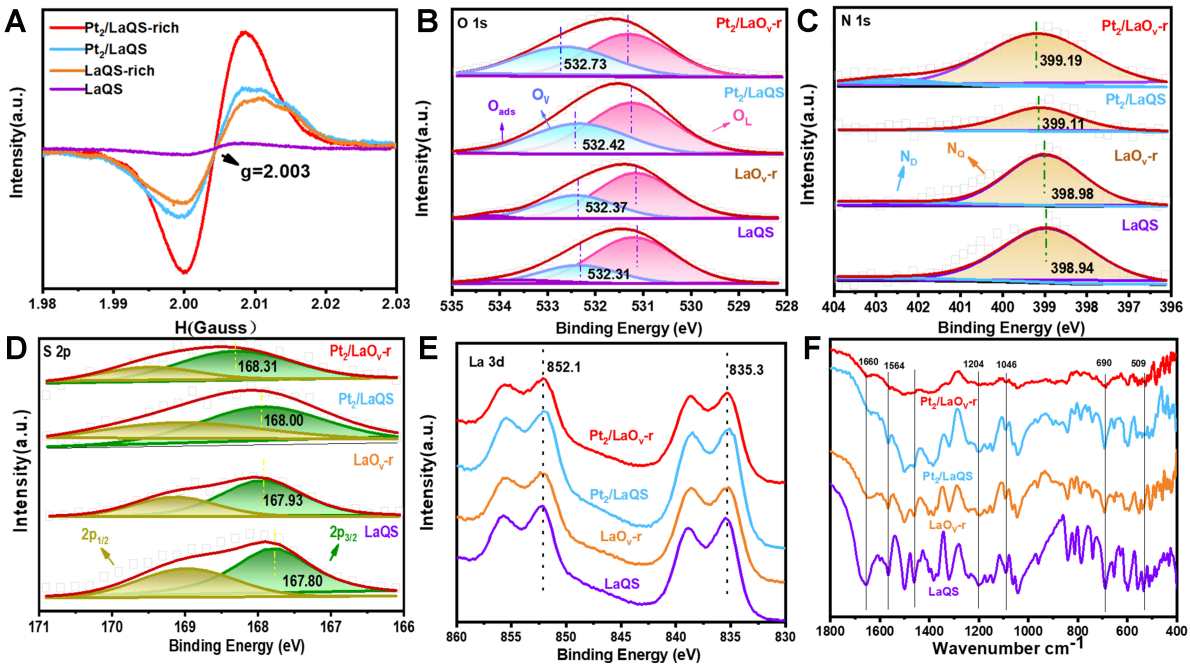

Figure 2. (A) EPR spectra of LaQS, LaO_V-r, Pt_2/LaQS and Pt_2/LaO_V-r; (B-E) XPS spectra of O 1s, N 1s, S 2p and La 3d of LaQS, LaO_V-r, Pt_2/LaQS and Pt_2/LaO_V-r; (F) IR spectra of LaQS, LaO_V-r, Pt_2/LaQS and Pt_2/LaO_V-r. EPR: Electron paramagnetic resonance; XPS: X-ray photoelectron spectroscopy; IR: infrared spectroscopy.

Catalytic properties

O_V promoted catalytic performance of ultrafine Pt NPs

Table 2 displays the comparative results of different catalysts. The catalytic activity of LaO_V-r support for EL is 0 at 130 °C, the same as the blank (Entries 1-2). The commercial Pt/C catalyst has a conversion of 50% and a selectivity of only 25% at 80 °C and 2 MPa H_2 (Entry 3). The reaction conversion of Pt_2/LaQS is only 31%, but its selectivity is increased to 99% (Entry 4). Although the catalytic conversion of Pt_2/LaQS is not as high as that of Pt/C, a higher selectivity is obtained, which may be due to the interaction of Pt with the support. Remarkably, under the same conditions, Pt_2/LaO_V-r has 99% conversion and 99% selectivity in the 4 h reaction (Entry 5); the yield is 13.3 and 3.2 times higher than those of commercial Pt/C and Pt_2/LaQS, respectively. The reaction conversion of Pt_1/LaO_V-r is 70% and the selectivity is 50% (Entry 6), probably because the Pt content reduction affects the LaO_V-r support thereby decreasing the catalytic activity of Pt_1/LaO_V-r [Supplementary Figures 2-6]. The product yield and selectivity of Pt_2/LaO_V-r remain hardly changed after three cycles (Entry 8). An absence of Pt in the reaction solution measured by ICP suggests that the interaction of Pt with LaO_V-r ensures the stability of Pt_2/LaO_V-r. By comparing the XPS spectra of O 1s after the cycles, the binding energy of O_V only decreased by 0.03 eV after cycles [Supplementary Figure 7]. Meanwhile, the O_V content only showed a minor decrease. This indicates that O_V remain relatively stable during cyclic reactions. Notably, the Pt_2/LaO_V-r catalyst has >99% yield of GVL after 36 h at room temperature of 25 °C (Entry 7). Compared with the Pt metal catalyst in the catalytic literature [Supplementary Table 1], the Pt_2/LaO_V-r catalyst in this study has higher performance and lower reaction conditions. This may be attributed to the fact that the Pt_2/LaO_V-r structure possesses more O_V, enabling better performance for the bifunctional catalyst with Lewis acidic and hydrogenation sites.

The synergy of O_V and Pt NPs for enhanced H_2 activation

H_2-TPD curves were examined to assess the H_2 adsorption capabilities of different catalysts [Figure 3A]. Compared to Pt_2/LaQS, Pt_2/LaO_V-r has a larger desorption peak at 217 °C. This suggests that the O_V rise

Table 2. Preparation of GVL from EL catalyzed by different catalysts[a]

Entry	Catalyst	Condition	Con (%)	Sel (%)
1	blank	130 °C	0	0
2	LaO_V-r	130 °C	0	0
3	Pt/C	80 °C	30	25
4	Pt_2/LaQS	80 °C	31	>99
5	Pt_2/LaO_V-r	80 °C	>99	>99
6	Pt_1/LaO_V-r	80 °C	70	50
7	Pt_2/LaO_V-r	25 °C	>99	>99
8	Pt_2/LaO_V-r[b]	70 °C	80	>99

Reaction conditions: [a]catalyst: 25 mg; 2-propanol, 8 mL; EL: 144 mg; H_2, 2 MPa; 4 h. [b]Catalyst: 25 mg; 2-propanol, 8 mL; EL: 144 mg; H_2, 2 MPa; 4 h; cycle 3 times. GVL: γ-valerolactone; EL: ethyl levulinate.

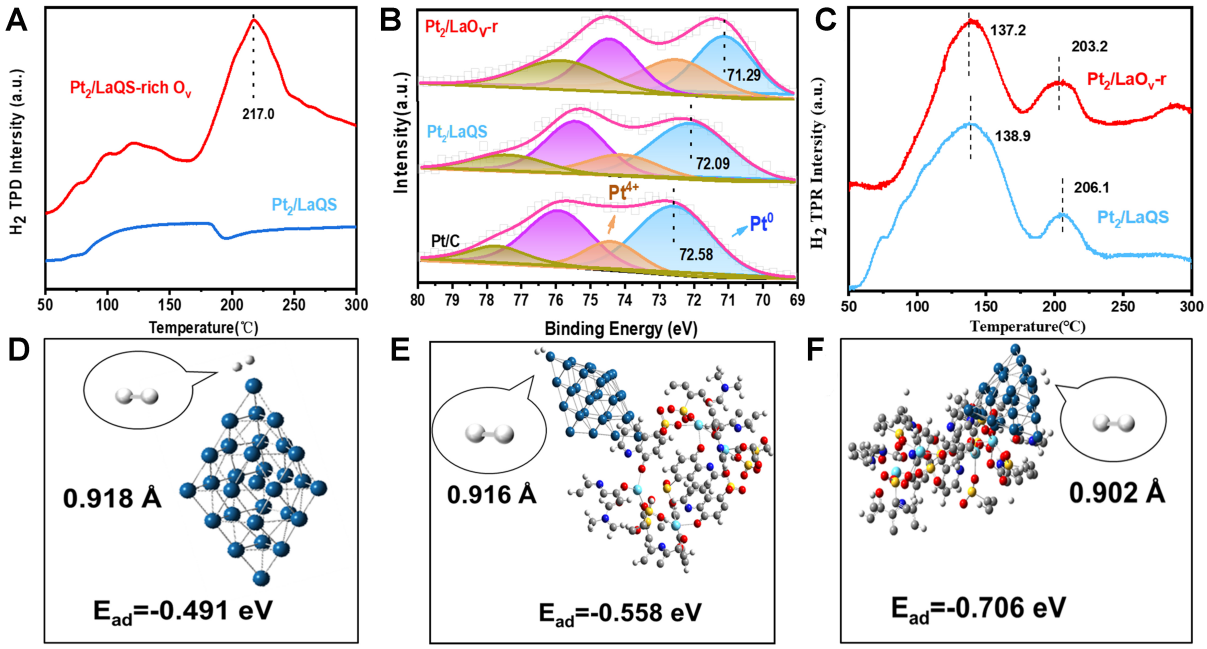

Figure 3. (A) H_2-TPD spectra of Pt_2/LaQS and Pt_2/LaO_V-r; (B) XPS spectra of Pt 4f of Pt/C, Pt_2/LaQS and Pt_2/LaO_V-r; (C) H_2-TPR spectra of Pt_2/LaQS and Pt_2/LaO_V-r; (D-F) H_2 adsorbed on Pt NPs, Pt sites on Pt_2/LaO_V-r and Pt_2/LaQS. TPD: Temperature-programmed desorption; XPS: X-ray photoelectron spectroscopy; TPR: temperature-programmed reduction; NPs: nanoparticles.

significantly enhances H_2 adsorption and the support with rich O_V in Pt_2/LaO_V-r exhibits a stronger interaction with the metal Pt NPs. The peak at 217 °C is notably pronounced in the Pt_2/LaO_V-r catalyst compared to the Pt_1/LaO_V-r catalyst with 1 wt% loading [Supplementary Figure 3], indicating an enhanced interaction between the support and Pt NPs with an increase of Pt loading, as supported by the Pt 4f XPS analysis in Figure 3B. Compared with 72.58 eV in Pt/C, the binding energy of Pt in Pt_2/LaQS is notably stronger [Figure 3B]. In Pt_2/LaQS, the binding energy of Pt is decreased to 72.09 eV, representing a reduction of 0.49 eV. This implies that electrons transfer from the LaQS to Pt, which increases the electron density of Pt NPs on Pt_2/LaQS. While in Pt_2/LaO_V-r, the binding energy is decreased to 71.29 eV, a substantial reduction of 0.8 eV. This suggests that an increase of O_V content causes more electron transfer from the LaQS to Pt, resulting in the highest electron density of Pt NPs on Pt_2/LaO_V-r. This enhances the Pt feedback to the H–H back-bonding orbitals, thereby reducing the hydrogen activation energy for adsorption. This improvement enhances the ability of H_2 to activate. The reduction behaviors of Pt_2/LaO_V-r

and Pt_2/LaQS were assessed using H_2-TPR [Figure 3C]. Compared with 138.9 and 206.1 °C for Pt_2/LaQS, the reduction peak temperature of Pt_2/LaO_V-r is lower shifted to 137.2 and 203.2 °C. This may be because the increase of O_V promotes the migration of oxygen[43], thus affecting the reduction performance of the catalyst. This elevated O_V in MOFs facilitates the interaction of Pt NPs with LaO_V-r support, consistent with the XPS analysis. Thus, the primary reason for the higher catalytic activity of Pt_2/LaO_V-r than Pt_2/LaQS is the elevated electron density resulting from the rich O_V.

The density-functional theory (DFT) calculation confirms the corollary that oxygen-rich vacancies promoted the invigoration of H_2 by the Pt NPs. Figure 3D illustrates the adsorption energy of pure Pt NPs for hydrogen (-0.491 eV). The modeled activation of H_2 by Pt NPs alone, as well as in Pt_2/LaQS, is shown in Figure 3E and F. The adsorption energies of Pt_2/LaO_V-r and Pt_2/LaQS for hydrogen (-0.558 and -0.706 eV) are smaller than that of the Pt NPs (-0.491 eV), suggesting that the association between the supporters (LaO_V-r and LaQS) and Pt NPs facilitates the adsorption and activation of H_2 with the Pt NPs. This also indicates that the interaction of O_V with Pt NPs in Pt_2/LaO_V-r promotes H_2 activation, which agrees with the characterization and the catalysis findings.

Synergistic promotion of EL activation and intermediate cyclization by O_V and Pt NPs

To explore the influence of acidic and basic sites on the EL hydrogenation reaction, Pt_2/LaO_V-r catalysis poisoning experiments were conducted. In Figure 4A, the addition of benzoic acid to poison the basic site results in a decrease of conversion and selectivity from 100% to 1% and 20%, respectively. This underscores the crucial role of the basic site as a promoter. Furthermore, the addition of potassium thiocyanate (KSCN) to poison the acidic site leads to an even more substantial reduction of conversion and selectivity to 0%. This indicates the essential nature of the acidic site as a catalytic site. In order to further study the effects of acidic and basic sites, NH_3-TPD and CO_2-TPD analyses were performed. The acidic sites were additionally analyzed through NH_3-TPD [Figure 4B]. As depicted, a new desorption peak emerges around 225 °C for Pt_2/LaQS and Pt_2/LaO_V-r in comparison to LaO_V-r, suggesting that the emergence of a new medium-strong Lewis acid site after Pt NPs loading is Pt^{4+}. Compared with 1,417.4 μmol/g for Pt_2/LaQS, the quantity of medium-strong acid in Pt_2/LaO_V-r is significantly increased to 1,803.6 μmol/g after the introduction of a large number of O_V, whereas Pt_1/LaO_V-r has a medium-strong acid amount of 1,561.5 μmol/g [Supplementary Table 2]. This implies that the abundance of O_V introduces additional acidic sites, further influencing the carbonyl activation capacity of the EL. This is consistent with the results of XPS analysis. Furthermore, this activation capacity is augmented with increasing the loading. In comparison to 24.82% of Pt^{4+} in Pt_2/LaQS, the introduction of O_V leads to a substantial increase of Pt^{4+} content (34.03%) in Pt_2/LaO_V-r. Consequently, ultrafine Pt NPs and a significant number of vacancies can function as mutually enhancing acidic activation sites, thereby improving the ability of the catalyst to activate the C=O on EL. Analyzing the basic sites through CO_2-TPD [Figure 4C], the adsorption peaks of the LaO_V-r carrier at 160 °C and Pt_2/LaO_V-r at 140 °C are inferred to be associated with the electron-rich N on the LaQS carrier. The reduction in electron cloud density of N, caused by the interaction of loaded Pt NPs with electron-rich N, leads to a decrease in its basicity. Regarding the LaO_V-r support, Pt_2/LaQS, and Pt_2/LaO_V-r possess a new medium-strong basic site around 220 °C, possibly attributed to the loaded metal Pt. After the substantial introduction of O_V, the quantity of medium-strong acid in Pt_1/LaO_V-r is increased to 1,133.9 μmol/g, compared to 812.1 μmol/g for Pt_2/LaQS, while the amount of medium-strong acid in Pt_2/LaO_V-r remains at 1,133.9 μmol/g. Compared to 812.1 μmol/g for Pt_2/LaQS, Pt_2/LaO_V-r experiences a substantial increase from 1,133.9 to 1,554.6 μmol/g in terms of medium-strong base [Supplementary Table 3]. Pt 4f XPS analysis reveals that the O_V rise results in more electron shift from the LaO_V-r supporter to Pt NPs compared with Pt_2/LaQS. Consequently, this leads to a much higher electron cloud density of Pt^0 from Pt_2/LaO_V-r, rendering it more basic. Moreover, this trend further intensifies with an increase in metal loading.

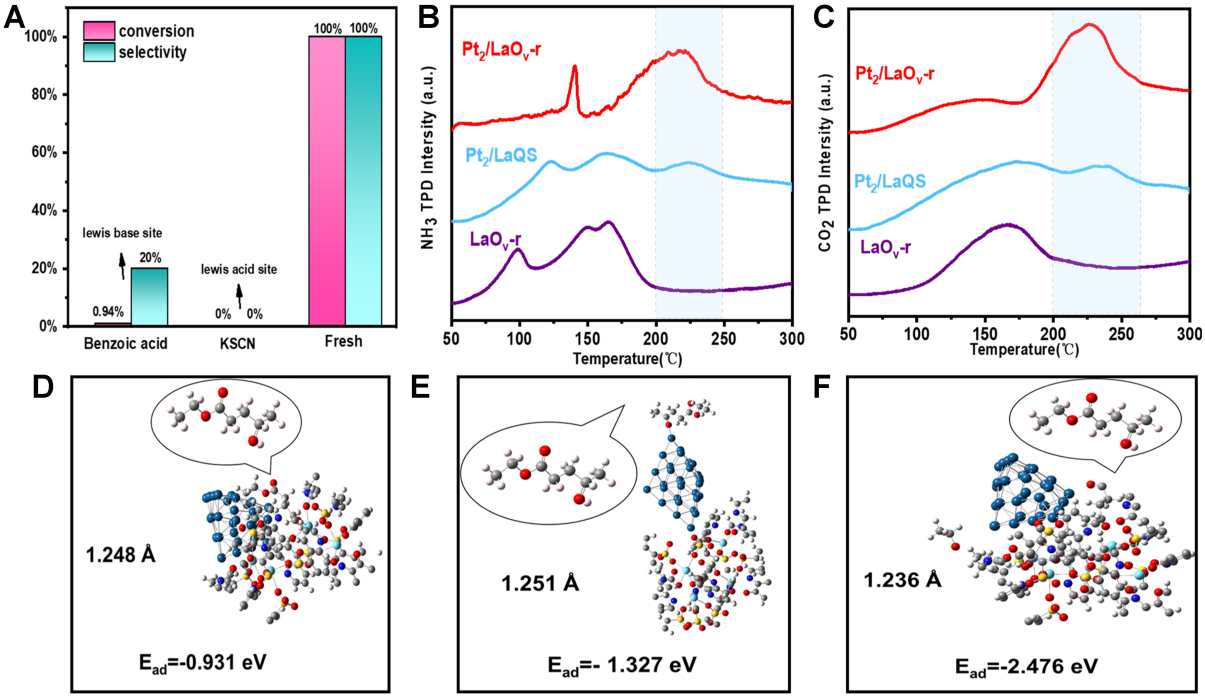

Figure 4. (A) Pt_2/LaO_V-r catalyzed poisoning experiments for EL hydrogenation; (B) CO_2-TPD curves of LaO_V-r, Pt_2/LaQS and Pt_2/LaO_V-r; (C) NH_3-TPD curves of LaO_V-r, Pt_2/LaQS and Pt_2/LaO_V-r; (D-F) EL adsorbed on O_V and Pt sites on Pt_2/LaO_V-r, Pt sites on Pt_2/LaQS. EL: Ethyl levulinate; TPD: temperature-programmed desorption.

To explore the activation effect of Pt loading on EL, DFT calculations were performed for Pt NPs and O_V in Pt_2/LaO_V-r. The adsorption of Pt NPs on EL in Pt_2/LaQS, and O_V and La^{3+} in LaO_V-r were performed [Figure 4D-F and Supplementary Figure 8]. Poisoning experiments in EL hydrogenation reveal that the acid sites are toxicated as a result of KSCN, resulting in zero transformation of EL [Figure 4A]. The Lewis acidic sites of the catalyst surface originate from Pt^{4+} in Pt NPs, La^{3+} in LaQS, and O_V. In Figure 3B, there was a higher energy of adsorption of ethyl acetylpropionate by Pt^{4+} in Pt_2/LaO_V-r (-1.327 eV) as compared to that by La^{3+} (-0.891 eV) and O_V (-0.931 eV), indicating that C=O in ethyl acetylpropionate is primarily being activated by Pt^{4+} in Pt_2/LaO_V-r. Moreover, the C=O bond length when adsorbed onto Pt^{4+} in Pt_2/LaQS (1.251 Å) is longer than that on La^{3+} (1.244 Å), O_V (1.248 Å), and free EL (1.222 Å), which further suggests EL adsorption on Pt^{4+} in Pt_2/LaQS. Simultaneously, NH_3-TPD analysis [Figure 4B] indicates that Pt^{4+}, which has a medium-strength acidic characteristic, is the primary site for EL activation. Furthermore, the commercial catalyst Pt/C exhibits a very low EL conversion (50%) and a poor GVL selectivity (25%) under identical conditions (Table 2, Entry 4). This is mainly attributed to Pt/C having a lower Pt^{4+} content of 23.38% than Pt_2/LaO_V-r (34.03%). Additionally, compared to 1.236 Å in Pt_2/LaQS [Figure 4D], the length of the bond of Pt^{4+} adsorbed C=O of EL in Pt_2/LaO_V-r is increased to 1.251 Å [Figure 4F]. This suggests that the interaction of O_V in LaO_V-r with Pt NPs promotes the activation of C=O on EL by Pt^{4+} in Pt_2/LaO_V-r.

Synergistic catalytic mechanism of O_V and Pt NPs

To explore the catalytic mechanism, *in situ* CO IR tests were conducted on Pt_2/LaQS and Pt_2/LaO_V-r catalysts. The absence of peaks below 2,000 cm^{-1} [Figure 5A and B] attributed to CO bridge adsorption on Pt^0[44,45] further supports the dispersion of Pt in NPs. This is due to the propensity for dipole-dipole interactions among neighboring CO adsorbed species on NPs. Simultaneously, the intensity of CO adsorption peaks on Pt_2/LaO_V-r is lower than that on Pt_2/LaQS, possibly due to the lower Pt^0 content in Pt_2/LaO_V-r. This aligns with the XPS analysis, where Pt^0 content in Pt_2/LaO_V-r (65.97%) is smaller than that in

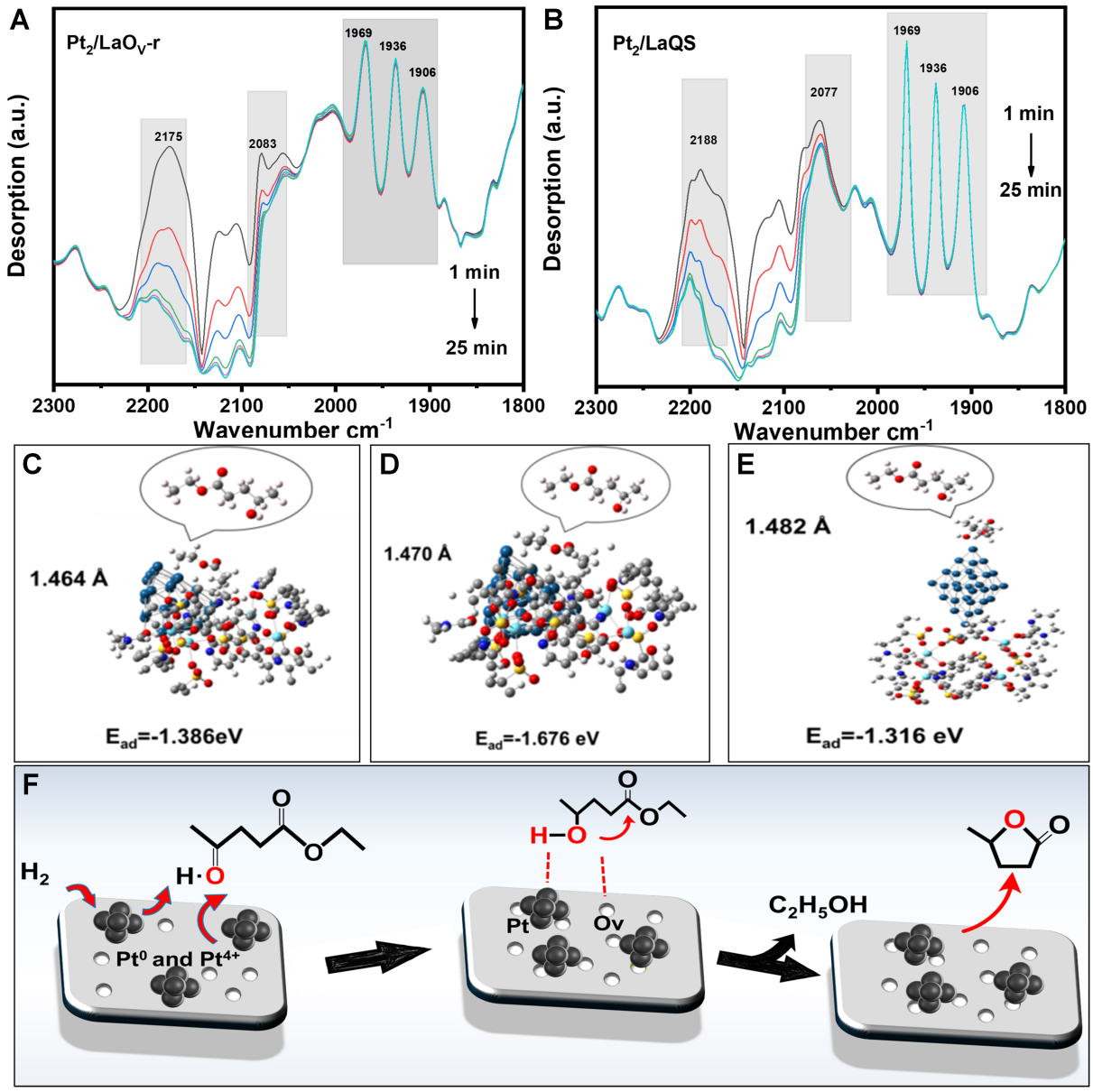

Figure 5. (A and B) *In situ* infrared spectra of CO desorption in Pt_2/LaQS and Pt_2/LaO_V-r; (C-E) 4-HPE adsorbed on La, O_V and Pt sites on Pt_2/LaO_V-r; (F) a proposed hydrogenation mechanism of EL to GVL. 4-HPE: 4-hydroxyvalerate; EL: ethyl levulinate; GVL: γ-valerolactone.

Pt_2/LaQS (73.18%). Compared with CO adsorption in Pt_2/LaQS catalyst (2,077 cm^{-1})[45], the adsorption peak in Pt_2/LaO_V-r is shifted to 2,083 cm^{-1}. This shift may be attributed to an increase in O_V in LaO_V-r, causing a decrease in the binding energy of Pt from 72.09 eV in Pt_2/LaQS to 71.29 eV in Pt_2/LaO_V-r. This implies that the increase in O_V causes LaO_V-r support to transfer more electrons onto the Pt NPs. The higher the electron density on Pt NPs means its stronger interaction with CO adsorption, resulting in a shift of the outgoing peak position to a lower wavenumber. Peak positions at higher wavenumbers of 2,188 and 2,175 cm^{-1} indicate linear adsorption of CO with $Pt^{\delta+}$ species in the oxidized state[46]. The red shift from 2,188 cm^{-1} of Pt_2/LaQS to 2,175 cm^{-1} of Pt_2/LaO_V-r indicates a high content of Pt species in its oxidized state, with O_V promoting an increase in Pt^{4+} electron density. This aligns with the XPS analysis, where the

introduction of O_V in Pt_2/LaO_V-r results in a significant increase in Pt^{4+} content from 24.82% (Pt_2/LaQS) to 34.03% (Pt_2/LaO_V-r). *In situ* IR results of CO indicate that the increased presence of O_V in LaO_V-r enhances both the electron cloud density on Pt NPs and the number of medium-strong acidic sites (Pt^{4+}), thereby improving the response to hydrogen and the activation capacity of EL.

Lewis acid plays a significant part in the molecular dehydrogenation reactions during the hydrogenation of ethyl acetylpropionate[47,48]. XPS and NH_3-TPD analyses reveal that the higher Pt^{4+} content in $Pt_2//LaO_V$-r corresponds to higher acidic strength, contributing significantly to the intra-molecular dehydrogenation of the intermediate 4-hydroxyvalerate (4-HPE). DFT calculations were performed for Pt^{4+}, La^{3+} and O_V adsorption on Pt_2/LaO_V-r for 4-HPE in order to further investigate the acidic site role in the dehydrogenation process of the intermediate [Figure 5C-E]. With excluding the effects of Pt for O_V and La elements in LaO_V-r, the effect of O_V for the Pt elements in Pt_2/LaQS is also excluded [Supplementary Figure 9]. For C–O adsorption in 4-HPE, compared with -1.386 and -1.316 eV of La^{3+} and Pt^{4+} on Pt_2/LaO_V-r, the adsorption energy of O_V on Pt_2/LaO_V-r is increased to -1.676 eV. This implies that the 4-HPE is predominantly adsorbed on O_V in Pt_2/LaO_V-r. This contrasts with the EL analysis of Pt^{4+} adsorption and activation in the medium-strong acidic site. This suggests that O_V in Pt_2/LaO_V-r exhibiting stronger affinity for 4-HPE promotes its adsorption and favors the subsequent dehydrogenation reaction. The above analysis also shows that O_V once again functions as acidic sites for catalysis. Consequently, the catalytic effect of the Pt_2/LaO_V-r catalyst is noteworthy with O_V playing a crucial role in enhancing the adsorption capacity of the intermediate.

The reaction mechanism is hypothesized for the catalytic hydrogenation of EL by Pt_2/LaO_V-r[47,48] [Figure 5F]. The catalytic hydrogenation of EL involves the hydrogenation of EL to 4-HPE and the intramolecular dehydrogenation of 4-HPE to GVL. The process necessitates a bifunctional catalyst with both Lewis acid and hydrogenation active sites. The combination of results from experiments and DFT calculations suggests that the synergistic interaction of O_V with Pt NPs on the Pt_2/LaO_V-r surface is essential for efficient transformation of EL to GVL. The characterization shows that O_V in Pt_2/LaO_V-r not only enhances the electron density of the Pt^0, but also increases the content of Pt^{4+} [Table 1]. H_2 moieties initially attached to the high-electron-density Pt^0 active sites are activated into hydrogen atoms. Both DFT and NH_3-TPD show that the Pt^{4+} sites were effective in adsorbing and activating C=O in EL. Subsequently, the activated hydrogen atoms attack the C=O group in the neighboring EL molecule, producing the 4-HPE. In the 4-HPE to GVL process, the acidic sites of O_V play a crucial role[47,48]. The DFT calculations reveal that -O-H in 4-HPE is adsorbed on the O_V site and the Pt^0 basic site, separately. This activates -O-H and facilitates the intramolecular ester exchange reaction to remove ethanol at the acid-base sites of the catalyst. The acid-base interaction facilitates the conversion of 4-HPE to GVL. Ultimately, GVL dissociates from the catalyst surface, and the active sites continue to be recycled. The synergistic effect of O_V and NPs on Pt_2/LaO_V-r not only enhances the adsorption capacity for substrates and generates 4-HPE, but also significantly promotes the dehydrogenation reaction of 4-HPE to GVL.

CONCLUSION

In this study, a simple solvent-induced O_V strategy was used to prepare bifunctional Pt_2/LaO_V-r catalyst with ultra-small Pt NPs (1.6 nm) and rich O_V. At an ambient temperature of 25 °C, the optimal Pt_2/LaO_V-r catalyst exhibits complete conversion of EL to GVL. At 80 °C, the yield of EL to GVL reached >99%, which is 3.2 and 13.3 fold higher than Pt_2/LaO_V and commercially available Pt/C catalysts, respectively. The high catalytic performance of Pt_2/LaO_V-r was attributed to the synergistic interaction between ultra-small Pt NPs and rich O_V. O_V not only increases Pt^0 electron cloud density and Pt^{4+} content of Pt NPs, but also introduces additional acidic catalytic sites. On the one hand, this enhances the activation of H_2 and EL. On the other

hand, it also promotes intramolecular dehydration of 4-HPE. Finally, the synergistic catalytic mechanism of O_V and Pt NPs on MOFs was also hypothesized through characterization and DFT calculations. This approach is an important guide for the development of vacancy-rich MOFs-based catalysts in the modulation of biomass catalytic conversion.

DECLARATIONS

Authors' contributions

Experiment performing, data analysis, results interpretation and manuscript drafting: Yan, W.
Data analysis and results discussion: Dao, Z.; Pu, S.; Yang, C.; Zhao, X.; Zhuang, C.
Manuscript revision, theoretical calculations, and administrative, technical and material support: Min, C.; Wang, Y.; Zhao, X. J.; Zou, X.

Availability of data and materials

The raw data supporting the findings of this study are available within this Article and its Supplementary Materials. Further data is available from the corresponding authors upon reasonable request.

Financial support and sponsorship

The authors gratefully acknowledge the supports from the National Natural Science Foundation of China (32360430, 22375031), Science and Technology Planning Project of Yunnan Province (202401BD070001-030, 202101BD070001-007), Young and Middle-aged Academic and Technical Leaders Project in Yunnan Province (202205AC160052), Jilin Natural Science Fund for Excellent Young Scholars (20230508116RC), and Fundamental Research Funds for the Central Universities (JGPY202103, 2412023YQ001).

Conflicts of interest

All authors declared that there are no conflicts of interest.

Ethical approval and consent to participate

Not applicable.

Consent for publication

Not applicable.

REFERENCES

1. Chen, J.; Sun, W.; Wang, Y.; Fang, W. Performant Au hydrogenation catalyst cooperated with Cu-doped Al_2O_3 for selective conversion of furfural to furfuryl alcohol at ambient pressure. *Green. Energy. Environ.* **2021**, *6*, 546-56. DOI
2. Sun, W.; Wu, S.; Lu, Y.; Wang, Y.; Cao, Q.; Fang, W. Effective control of particle size and electron density of Pd/C and Sn-Pd/C nanocatalysts for vanillin production via base-free oxidation. *ACS. Catal.* **2020**, *10*, 7699-709. DOI
3. Wei, Z.; Li, X.; Deng, J.; Wang, J.; Li, H.; Wang, Y. Improved catalytic activity and stability for hydrogenation of levulinic acid by Ru/N-doped hierarchically porous carbon. *Mol. Catal.* **2018**, *448*, 100-7. DOI
4. Yoshida, R.; Sun, D.; Yamada, Y.; Sato, S. Stable Cu-Ni/SiO_2 catalysts prepared by using citric acid-assisted impregnation for vapor-phase hydrogenation of levulinic acid. *Mol. Catal.* **2018**, *454*, 70-6. DOI
5. Gadamsetti, S.; Mathangi, N.; Hussain, S.; Kumar, V. V.; Chary, K. V. R. Vapor phase esterification of levulinic acid catalyzed by γ-Al_2O_3 supported molybdenum phosphate catalysts. *Mol. Catal.* **2018**, *451*, 192-9. DOI
6. Liguori, F.; Moreno-marrodan, C.; Barbaro, P. Environmentally friendly synthesis of γ-valerolactone by direct catalytic conversion of renewable sources. *ACS. Catal.* **2015**, *5*, 1882-94. DOI
7. Wang, Y.; Gai, Y.; Li, Y.; Li, C.; Li, Z.; Wang, X. SARS-CoV-2 has the advantage of competing the iMet-tRNAs with human hosts to allow efficient translation. *Mol. Genet. Genomics.* **2021**, *296*, 113-8. DOI PubMed PMC
8. Zhao, D.; Wang, Y.; Delbecq, F.; Len, C. Continuous flow conversion of alkyl levulinates into γ-valerolactone in the presence of Ru/C as catalyst. *Mol. Catal.* **2019**, *475*, 110456. DOI

9. Cao, W.; Lin, L.; Qi, H.; et al. In-situ synthesis of single-atom Ir by utilizing metal-organic frameworks: an acid-resistant catalyst for hydrogenation of levulinic acid to γ-valerolactone. *J. Catal.* **2019**, *373*, 161-72. DOI
10. Li, W.; Cai, Z.; Li, H.; et al. Hf-based metal organic frameworks as bifunctional catalysts for the one-pot conversion of furfural to γ-valerolactone. *Mol. Catal.* **2019**, *472*, 17-26. DOI
11. Wettstein, S. G.; Bond, J. Q.; Alonso, D. M.; Pham, H. N.; Datye, A. K.; Dumesic, J. A. RuSn bimetallic catalysts for selective hydrogenation of levulinic acid to γ-valerolactone. *Appl. Catal. B. Environ.* **2012**, *117-8*, 321-9. DOI
12. Tan, J.; Cui, J.; Cui, X.; et al. Graphene-modified Ru nanocatalyst for low-temperature hydrogenation of carbonyl groups. *ACS. Catal.* **2015**, *5*, 7379-84. DOI
13. Song, S.; Yao, S.; Cao, J.; et al. Heterostructured Ni/NiO composite as a robust catalyst for the hydrogenation of levulinic acid to γ-valerolactone. *Appl. Catal. B. Environ.* **2017**, *217*, 115-24. DOI
14. Huang, X.; Liu, K.; Vrijburg, W. L.; et al. Hydrogenation of levulinic acid to γ-valerolactone over Fe-Re/TiO_2 catalysts. *Appl. Catal. B. Environ.* **2020**, *278*, 119314. DOI
15. Filho, J. B.; Rios, R. D.; Bruziquesi, C. G.; et al. A promising approach to transform levulinic acid into γ-valerolactone using niobic acid photocatalyst and the accumulated electron transfer technique. *Appl. Catal. B. Environ.* **2021**, *285*, 119814. DOI
16. Abdelrahman, O. A.; Heyden, A.; Bond, J. Q. Analysis of kinetics and reaction pathways in the aqueous-phase hydrogenation of levulinic acid to form γ-valerolactone over Ru/C. *ACS. Catal.* **2014**, *4*, 1171-81. DOI
17. Lomate, S.; Sultana, A.; Fujitani, T. Vapor phase catalytic transfer hydrogenation (CTH) of levulinic acid to γ-valerolactone over copper supported catalysts using formic acid as hydrogen source. *Catal. Lett.* **2018**, *148*, 348-58. DOI
18. Hao, P.; Schwartz, D. K.; Medlin, J. W. Effect of surface hydrophobicity of Pd/Al_2O_3 on vanillin hydrodeoxygenation in a water/oil system. *ACS. Catal.* **2018**, *8*, 11165-73. DOI
19. Mostofian, B.; Cai, C. M.; Smith, M. D.; et al. Local phase separation of co-solvents enhances pretreatment of biomass for bioenergy applications. *J. Am. Chem. Soc.* **2016**, *138*, 10869-78. DOI PubMed
20. Pera-Titus, M.; Leclercq, L.; Clacens, J. M.; De, C. F.; Nardello-Rataj, V. Pickering interfacial catalysis for biphasic systems: from emulsion design to green reactions. *Angew. Chem. Int. Ed. Engl.* **2015**, *54*, 2006-21. DOI PubMed
21. Lan, Y.; He, H.; Liu, C.; et al. Ultrasmall Pd nanocrystals confined into co-based metal organic framework-decorated MXene nanoarchitectures for efficient methanol electrooxidation. *J. Power. Sources.* **2024**, *603*, 234438. DOI
22. Kim, J.; Han, J. Simulation study of a strategy to produce gamma-valerolactone from ethyl levulinate. *Energy* **2018**, *163*, 986-91. DOI
23. Vu, H. T.; Harth, F. M.; Wilde, N. Silylated zeolites with enhanced hydrothermal stability for the aqueous-phase hydrogenation of levulinic acid to γ-valerolactone. *Front. Chem.* **2018**, *6*, 143. DOI PubMed PMC
24. Mizugaki, T.; Nagatsu, Y.; Togo, K.; et al. Selective hydrogenation of levulinic acid to 1,4-pentanediol in water using a hydroxyapatite-supported Pt–Mo bimetallic catalyst. *Green. Chem.* **2015**, *17*, 5136-9. DOI
25. Nemanashi, M.; Noh, J.; Meijboom, R. Hydrogenation of biomass-derived levulinic acid to γ-valerolactone catalyzed by mesoporous supported dendrimer-derived Ru and Pt catalysts: an alternative method for the production of renewable biofuels. *Appl. Catal. A. Gen.* **2018**, *550*, 77-89. DOI
26. Al-naji, M.; Popova, M.; Chen, Z.; Wilde, N.; Gläser, R. Aqueous-phase hydrogenation of levulinic acid using formic acid as a sustainable reducing agent over Pt catalysts supported on mesoporous zirconia. *ACS. Sustain. Chem. Eng.* **2020**, *8*, 393-402. DOI
27. Serrano-ruiz, J. C.; Wang, D.; Dumesic, J. A. Catalytic upgrading of levulinic acid to 5-nonanone. *Green. Chem.* **2010**, *12*, 574. DOI
28. He, J.; Li, H.; Xu, Y.; Yang, S. Dual acidic mesoporous KIT silicates enable one-pot production of γ-valerolactone from biomass derivatives via cascade reactions. *Renew. Energy.* **2020**, *146*, 359-70. DOI
29. Winoto, H. P.; Ahn, B. S.; Jae, J. Production of γ-valerolactone from furfural by a single-step process using Sn-Al-beta zeolites: optimizing the catalyst acid properties and process conditions. *J. Ind. Eng. Chem.* **2016**, *40*, 62-71. DOI
30. Liu, L.; Corma, A. Metal catalysts for heterogeneous catalysis: from single atoms to nanoclusters and nanoparticles. *Chem. Rev.* **2018**, *118*, 4981-5079. DOI PubMed PMC
31. Vinokurov, V.; Glotov, A.; Chudakov, Y.; et al. Core/shell ruthenium–halloysite nanocatalysts for hydrogenation of phenol. *Ind. Eng. Chem. Res.* **2017**, *56*, 14043-52. DOI
32. Jiang, W.; Cao, J.; Zhu, C.; et al. Catalytic hydrogenation of aromatic ring over ruthenium nanoparticles supported on α-Al_2O_3 at room temperature. *Appl. Catal. B. Environ.* **2022**, *307*, 121137. DOI
33. Bavykina, A.; Kolobov, N.; Khan, I. S.; Bau, J. A.; Ramirez, A.; Gascon, J. Metal-organic frameworks in heterogeneous catalysis: recent progress, new trends, and future perspectives. *Chem. Rev.* **2020**, *120*, 8468-535. DOI PubMed
34. Yang, Q.; Xu, Q.; Jiang, H. L. Metal-organic frameworks meet metal nanoparticles: synergistic effect for enhanced catalysis. *Chem. Soc. Rev.* **2017**, *46*, 4774-808. DOI PubMed
35. Mukoyoshi, M.; Kitagawa, H. Nanoparticle/metal-organic framework hybrid catalysts: elucidating the role of the MOF. *Chem. Commun.* **2022**, *58*, 10757-67. DOI PubMed
36. Shearer, G. C.; Chavan, S.; Bordiga, S.; Svelle, S.; Olsbye, U.; Lillerud, K. P. Defect engineering: tuning the porosity and composition of the metal–organic framework UiO-66 via modulated synthesis. *Chem. Mater.* **2016**, *28*, 3749-61. DOI
37. Xu, W.; Zhang, Y.; Wang, J.; et al. Defects engineering simultaneously enhances activity and recyclability of MOFs in selective hydrogenation of biomass. *Nat. Commun.* **2022**, *13*, 2068. DOI PubMed PMC
38. Long, J.; Yao, Q.; Zhang, X.; Wu, H.; Lu, Z. Defects engineering of metal-organic framework immobilized Ni-$La(OH)_3$ nanoparticles for enhanced hydrogen production. *Appl. Catal. B. Environ.* **2023**, *320*, 121989. DOI

39. Wang, W.; Sheng, T.; Chen, S.; et al. Defect engineering of metal-organic framework for highly efficient hydrodeoxygenation of lignin derivates in water. *Chem. Eng. J.* **2023**, *453*, 139711. DOI
40. Cui, Y.; Cui, X.; Yang, G.; et al. High CO_2 adsorption of ultra-small Zr-MOF nanocrystals synthesized by modulation method boosts the CO_2/CH_4 separation performance of mixed-matrix membranes. *J. Membr. Sci.* **2024**, *689*, 122174. DOI
41. Zhao, X.; Sun, L.; Zhai, Z.; et al. An ultrastable La-MOF for catalytic hydrogen transfer of furfural: *in situ* activation of the surface. *Nanoscale* **2023**, *15*, 6645-54. DOI PubMed
42. Zhang, J.; Li, C.; Chen, X.; et al. Promotional effects of magnesia on catalytic performance of Pt/SiO_2 in hydrogenolysis of dibenzofuran. *J. Catal.* **2019**, *371*, 346-56. DOI
43. Zhang, H.; Wang, J.; Zhang, Y.; et al. A study on H_2-TPR of $Pt/Ce_{0.27}Zr_{0.73}O_2$ and $Pt/Ce_{0.27}Zr_{0.70}La_{0.03}O_x$ for soot oxidation. *Appl. Surf. Sci.* **2016**, *377*, 48-55. DOI
44. Qiao, B.; Wang, A.; Yang, X.; et al. Single-atom catalysis of CO oxidation using Pt_1/FeO_x. *Nat. Chem.* **2011**, *3*, 634-41. DOI
45. Pozdnyakova, O.; Teschner, D.; Wootsch, A.; et al. Preferential CO oxidation in hydrogen (PROX) on ceria-supported catalysts, part I: oxidation state and surface species on Pt/CeO_2 under reaction conditions. *J. Catal.* **2006**, *237*, 1-16. DOI
46. Cheah, S. K.; Bernardet, V. P.; Franco, A. A.; Lemaire, O.; Gelin, P. Study of CO and hydrogen interactions on carbon-supported Pt nanoparticles by quadrupole mass spectrometry and operando diffuse reflectance FTIR spectroscopy. *J. Phys. Chem. C.* **2013**, *117*, 22756-67. DOI
47. Gupta, S. S. R.; Kantam, M. L. Selective hydrogenation of levulinic acid into γ-valerolactone over Cu/Ni hydrotalcite-derived catalyst. *Catal. Today.* **2018**, *309*, 189-94. DOI
48. Lu, Y.; Wang, Y.; Tang, Q.; Cao, Q.; Fang, W. Synergy in Sn-Mn oxide boosting the hydrogenation catalysis of supported Pt nanoparticles for selective conversion of levulinic acid. *Appl. Catal. B. Environ.* **2022**, *300*, 120746. DOI

Wei Yan

Wei Yan is currently pursuing his master's degree at the School of Materials and Chemical Engineering, Southwest Forestry University. His main research interests include metal-organic skeleton-derived materials catalysts and their applications in biomass catalytic conversion.

Ying Wang

Ying Wang received her Ph.D. from Jilin University in 2009. She has worked at Southwest Forestry University since then. Her current research interests focus on the design and synthesis of porous catalytic materials.

Xu Zhao

Xu Zhao graduated with a master's degree from Southwest Forestry University in 2023 and entered Northeast Normal University in September of the same year to pursue a doctoral degree.

Siyi Pu

Siyi Pu is a postgraduate student at the School of Materials and Chemical Engineering, Southwest Forestry University, with a major research interest in porous functional catalysts and their applications in catalytic conversion of biomass.

Chunyan Yang

Chunyan Yang graduated from Southwest Forestry University with a master's degree in 2024 and entered Soochow University in September of the same year to pursue her Ph.D.

Zirui Dao

Zirui Dao graduated with a master's degree from Southwest Forestry University in 2024, supervised by Prof Changfu Zhuang. His research interests are metal-organic framework-derived materials and their applications in biomass catalysis.

Changfu Zhuang

Changfu Zhuang received his Ph.D. from Jilin University in 2010. He has worked at Southwest Forestry University since then. His current research interests are focused on the design and synthesis of porous catalytic materials.

Chungang Min

Chungang Min received his Ph.D. from Jilin University in 2011. After that, he worked in Kunming University of Science and Technology. His current research interests focus on computational simulation of electrocatalytic materials.

Xiao-Jun Zhao

Xiao-Jun Zhao received his Ph.D. from Jilin University in 2009 and worked there until 2018. He then joined Hainan University. His current research interests focus on the design and synthesis of porous electro- and photoelectro-catalytic materials.

Xiaoqin Zou

Xiaoqin Zou obtained his Ph.D. from The University of Caen (France) in 2012. After completing postdoctoral research in The University of California at Berkeley (USA) from 2013 to 2015, he was directly appointed as a full professor in Northeast Normal University (China). His research interests focus on designing novel porous materials for separation membranes.